

Chapter 1

Introduction to X-Ray Absorption Spectroscopy

Claudia S. Schnohr and Mark C. Ridgway

X-ray Absorption Spectroscopy (XAS) is a well-established analytical technique used extensively for the characterization of semiconductors in solid or liquid, crystalline or amorphous, bulk or nanoscale form. With this chapter, we provide a brief introduction to XAS, covering both theory and experiment, while we refer to more comprehensive texts for greater detail about this continually evolving technique. The chapter thus is a starting point upon which subsequent chapters build as they demonstrate the broad-ranging applications of XAS to semiconductors materials.

1.1 Basic Principle

X-ray absorption spectroscopy (XAS) measures the energy-dependent fine structure of the X-ray absorption coefficient near the absorption edge of a particular element. Detailed discussions of both theoretical and experimental aspects of XAS can be found in [1–5].

1.1.1 X-Ray Absorption

If X-rays of intensity I_0 are incident on a sample, as shown schematically in Fig. 1.1a, the extent of absorption depends on the photon energy E and sample thickness t .

C.S. Schnohr (✉)

Institut für Festkörperphysik, Friedrich-Schiller-Universität Jena,
Max-Wien-Platz 1, 07743 Jena, Germany
e-mail: c.schnohr@uni-jena.de

M.C. Ridgway

Department of Electronic Materials Engineering, Australian National University,
Canberra, ACT 0200, Australia
e-mail: mark.ridgway@anu.edu.au

© Springer-Verlag Berlin Heidelberg 2015

C.S. Schnohr and M.C. Ridgway (eds.), *X-Ray Absorption Spectroscopy of Semiconductors*, Springer Series in Optical Sciences 190,
DOI 10.1007/978-3-662-44362-0_1

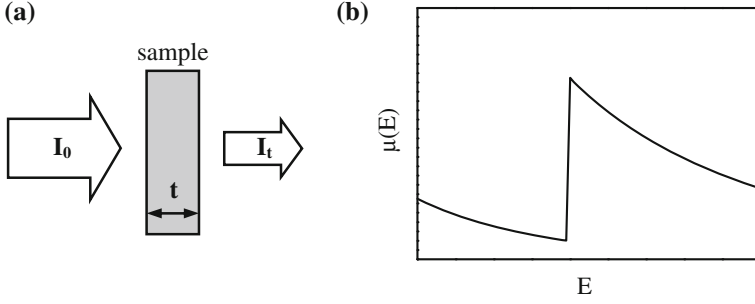


Fig. 1.1 **a** Schematic of incident and transmitted X-ray beam and **b** absorption coefficient $\mu(E)$ versus photon energy E around an absorption edge

According to Beer's Law, the transmitted intensity I_t is

$$I_t(t) = I_0 e^{-\mu(E)t} \quad (1.1)$$

where $\mu(E)$ is the energy-dependent X-ray absorption coefficient. Over large energy regions, $\mu(E)$ is a smooth function of the photon energy, varying approximately as $\mu(E) \sim dZ^4/mE^3$ [6]. Here d denotes the target density while Z and m are the atomic number and mass, respectively. Thus, $\mu(E)$ decreases with increasing photon energy. If the latter equals or exceeds the binding energy of a core electron, however, a new absorption channel is available in which the photon is annihilated thereby creating a photoelectron and a core-hole. This leads to a sharp increase in absorption coefficient as shown schematically in Fig. 1.1b. Above the absorption edge, the difference between the photon energy and the binding energy is converted into kinetic energy of the photoelectron and $\mu(E)$ continues to decrease with increasing photon energy. After a short time of the order of 10^{-15} s, the core-hole is filled by an electron from a higher energy state. The corresponding energy difference is released mainly via fluorescence X-ray or Auger electron emission [4].

1.1.2 Absorption Fine Structure

According to quantum mechanical perturbation theory, the transition rate between the core level and the final state is proportional to the product of the squared modulus of the matrix element M and the density of states ρ

$$\mu \propto |M|^2 \rho \propto |\langle f | H_p | i \rangle|^2 \rho \quad (1.2)$$

$|i\rangle$ and $|f\rangle$ denote the initial and final state, respectively, and H_p represents the interaction Hamiltonian that causes the transition, here the electromagnetic field of the X-ray photon [2]. Both factors can now cause a modulation of the absorption

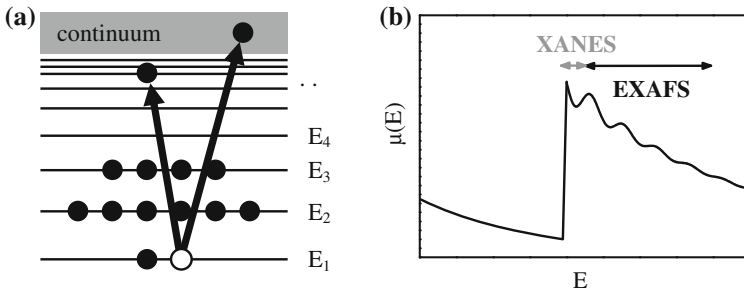
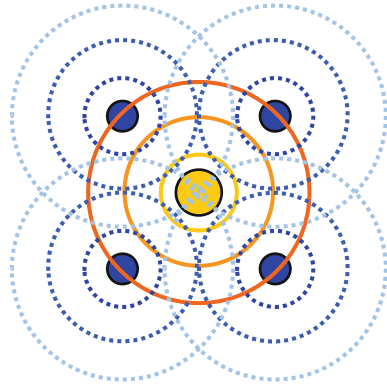


Fig. 1.2 **a** Schematic of the absorption process and **b** absorption coefficient $\mu(E)$ versus photon energy E including the fine structure above the edge divided into the XANES and EXAFS regions

Fig. 1.3 Schematic showing the absorbing atom (yellow) and its first nearest neighbors (blue). An interference pattern is created by the outgoing (solid orange lines) and reflected (dashed blue lines) photoelectron waves



coefficient thus creating the X-ray absorption fine structure (XAFS). At the smallest X-ray energies for which the photon can be absorbed, the photoelectron will be excited to unoccupied bound states of the absorbing atom as shown schematically in Fig. 1.2a. This can lead to a strong increase of the absorption coefficient at particular X-ray energies corresponding to the energy difference between the core level and the unoccupied states. For higher X-ray energies, the photoelectron is promoted to a free or continuum state. The wave thus created propagates outwards and is scattered at neighboring atoms [7] as shown schematically in Fig. 1.3. The outgoing and scattered waves interfere in a manner that depends on the geometry of the absorber environment and on the photoelectron wavelength. The latter is inversely proportional to the photoelectron momentum and therefore changes with photon energy. Thus, the final state is an energy-dependent superposition of outgoing and scattered waves. Because the initial state is highly localized at the absorbing atom, the matrix element M in (1.2) depends on the magnitude of the final state wave function at the site of the absorbing atom. Constructive or destructive interference of outgoing and scattered waves thus increases or decreases the absorption probability, creating an energy-dependent fine structure of the absorption coefficient. Figure 1.2b schematically shows the $\mu(E)$ fine structure as a function of photon energy. Two regions are commonly distinguished,

namely the X-ray absorption near edge structure (XANES) and the extended X-ray absorption fine structure (EXAFS).

1.1.2.1 XANES

The region very close to the absorption edge is characterized by transitions of the photoelectron to unoccupied bound states. XANES is therefore sensitive to the chemical bonding, exhibiting for example characteristic features for different oxidation states of the absorbing atom [4]. The XANES features are also influenced by strong multiple scattering effects which depend on the three-dimensional geometry of the crystal structure. This provides a means of distinguishing between different crystal phases [2]. Theoretical calculations of the fine structure in this region are complex and the accuracy of such simulations is still limited although significant progress has been made over recent years [8, 9]. Therefore, analysis typically compares the measured spectra to those of known standards and quantifies the ratios by which these standards are present in the sample using linear combination fitting. Often, the XANES region is also referred to as the near edge X-ray absorption fine structure (NEXAFS).

1.1.2.2 EXAFS

For photon energies higher than ~ 30 eV above the edge, the photoelectron is promoted to a free or continuum state. EXAFS is thus independent of chemical bonding and depends on the atomic arrangement around the absorber. It contains information about the coordination number, interatomic distances and structural and thermal disorder around a particular atomic species [7]. EXAFS does not require long-range order and is applicable to a wide range of ordered and disordered materials therefore providing a powerful tool for structural analysis. Theoretical calculations of the fine structure in the EXAFS region have also improved enormously during the last two decades and simulations with sufficient accuracy are now available [7, 9]. Nevertheless, the measurement of suitable standards still constitutes an important part of the experimental procedure.

1.2 Theoretical Description

1.2.1 Dipole Approximation

The Hamiltonian H_p in (1.2) describes the interaction of the electromagnetic field of the X-ray photon with the absorbing atom. It is proportional to the scalar product of the vector potential \vec{A} of the X-ray field and the electron momentum operator

\vec{p} , $H_p \propto \vec{A} \cdot \vec{p}$. In principle, this is a many-body problem where all electrons of the absorbing atom would have to be considered. Practically, however, it is usually assumed that only one electron is involved in the transition and corrections due to many-body effects are added at a later stage. Using this one-electron approximation together with the dipole approximation for $\vec{A} \cdot \vec{p}$ yields

$$\mu \propto |\langle f | \hat{e} \cdot \vec{r} | i \rangle|^2 \rho \quad (1.3)$$

where \hat{e} denotes the X-ray polarization vector [2, 5]. In most cases the dipole approximation is sufficient, however, quadrupole interactions may become important for high Z elements and L -edges [2].

Usually, synchrotron radiation is linearly polarized in the horizontal plane [2]. The matrix element in (1.3) therefore depends on the orientation of the line connecting absorber and scattering atom with respect to the X-ray polarization. In randomly oriented samples or in materials with cubic symmetry this angular dependence is averaged out. In contrast, the orientation dependence must be taken into account for single crystals or samples with a preferred particle or grain orientation. If unwanted, this X-ray linear dichroism can be averaged out experimentally by magic angle spinning of the sample [2]. It can, however, also be used intentionally as an additional source of information by performing systematic angle-dependent XAS measurements.

The matrix element in (1.3) is further subject to the well-known selection rules for transitions induced by electromagnetic radiation, i.e. $\Delta l = \pm 1$ and $\Delta m = 0, \pm 1$ for electric dipole interactions. Here, l and m denote the orbital angular momentum quantum number and its projection on the quantization axis, respectively [5]. The initial core state of the electron is to a good approximation given by an atomic-like state with well-defined quantum numbers l and m . In contrast, the final state is usually a superposition of wavefunctions with different values of l and m and only the fraction with the appropriate symmetry is of relevance for the transition [2]. Thus, for K - and L_1 -edges (s states with $l = 0$) transitions occur only to final states containing p symmetry while for L_2 - and L_3 -edges (p states with $l = 1$) transitions are only allowed to final states containing s or d symmetry.

1.2.2 Quasi-Particle Model

While the initial state is well approximated by an atomic-like state, the final state is an excited state characterized by the presence of a core-hole ('final state rule'). In the quasi-particle model these final states Ψ_f are eigenstates of a Dyson equation¹

$$h' \Psi_f = \left[\frac{p^2}{2m} + V' + \Sigma(E_f) \right] \Psi_f = E_f \Psi_f \quad (1.4)$$

¹ The analog of the Schrödinger equation for excited states.

where E_f denotes the energy of the photoelectron in the final state. The non-Hermitian Hamiltonian h' of the final state is characterized by the Coulomb potential V' calculated in the presence of a screened core-hole and by the complex valued and energy-dependent self-energy $\Sigma(E_f)$ which incorporates many-body effects and extrinsic inelastic losses [8]. The latter refer to losses during the propagation of the photoelectron and include excitations such as plasmons or electron-hole pairs and inelastic scattering in which the photoelectron loses energy [7]. The non-hermicity of h' corresponds to the complex nature of the eigenvalues E_f and is responsible for the finite lifetime of the final state [2]. Relativistic effects become important in the treatment of the initial atomic core states, especially for high elements, but have only weak effects on the propagation and scattering of the photoelectron in the final state [9].

1.2.3 Multiple Scattering Approach

The multiple scattering approach now separates the potential in (1.4) into individual contributions $v_{\vec{R}}$ localized at each atomic site \vec{R} [8]

$$V' + \Sigma(E_f) = \sum_{\vec{R}} v_{\vec{R}}(\vec{r} - \vec{R}) \quad (1.5)$$

For electrons with energies of several eV or more above the threshold, the scattering depends mostly on the potential in the core of the neighboring atom which is approximately spherical [9]. The “muffin-tin” approximation therefore assumes spherically symmetric atomic potentials out to a finite radius and a constant potential in between the atoms. The approximation is a good description for close-packed structures but works less well for open structures. Deviations are most prominent for small anisotropic systems close to the absorption threshold [2, 9].

Despite this approximation, the calculation of final states turns out to be computationally demanding and very often impractical. The multiple scattering approach therefore makes use of the photoelectron Green’s function or propagator \mathbf{G} in real space. Applying the identity

$$-\frac{1}{\pi} \text{Im} \mathbf{G} = \sum_f |f\rangle \delta(E + E_i - E_f) \langle f| \quad (1.6)$$

where E and E_i denote photon energy and electron energy in the initial state, respectively, (1.3) can be written as [2]

$$\begin{aligned} \mu &\propto \sum_f \langle i | \hat{\epsilon} \cdot \vec{r}' | f \rangle \delta(E + E_i - E_f) \langle f | \hat{\epsilon} \cdot \vec{r} | i \rangle \\ &\propto \text{Im} \langle i | \hat{\epsilon} \cdot \vec{r}' \mathbf{G} \hat{\epsilon} \cdot \vec{r} | i \rangle \end{aligned} \quad (1.7)$$

The propagator \mathbf{G} can be separated into a contribution \mathbf{G}^c stemming from the central atom and a contribution \mathbf{G}^{sc} due to multiple scattering from the environment, $\mathbf{G} = \mathbf{G}^c + \mathbf{G}^{sc}$. The nature of these contributions then allows expressing μ in terms of an atomic background μ_0 of the embedded absorber and the fine structure χ due to multiple scattering from the environment, $\mu = \mu_0(1 + \chi)$ [7]. Within this framework, the fine structure component is now given by

$$\chi = \text{Im } e^{i\delta} \left[\mathbf{1} - \mathbf{G}^0 \mathbf{T} \right]^{-1} \mathbf{G}^0 e^{i\delta'} \quad (1.8)$$

where \mathbf{G}^0 denotes the free particle propagator and \mathbf{T} represents the scattering matrix while δ and δ' are partial-wave phase shifts [7, 8]. The matrix term in (1.8) can be written as a series expansion

$$\left[\mathbf{1} - \mathbf{G}^0 \mathbf{T} \right]^{-1} \mathbf{G}^0 = \mathbf{G}^0 \mathbf{T} \mathbf{G}^0 + \mathbf{G}^0 \mathbf{T} \mathbf{G}^0 \mathbf{T} \mathbf{G}^0 + \dots \quad (1.9)$$

where the first term is missing due to the definition of \mathbf{G}^0 [7]. The fine structure contribution can thus be understood as the sum of individual scattering contributions arising from all possible paths of the photoelectron from the absorbing atom and back. The first, second, ... term in (1.9) correspond to single, double, ... scattering at surrounding atoms. The advantages of this multiple scattering Green's function formalism lie in the fact that it treats XANES and EXAFS within the same unified theory, that it avoids explicit calculation of the final state wave functions and that it naturally incorporates inelastic losses and other quasi-particle effects [7]. As an alternative to the path expansion, the fine structure contribution can also be expressed as the sum of irreducible n -body interactions which contain all scattering contributions due to a particular arrangement of n atoms including the absorber [10, 11]. This approach is directly related to the n -body distribution functions and is thus particularly suited for the study of highly disordered systems (see Chap. 9).

1.2.4 XANES

In the XANES region, the multiple scattering path expansion of (1.9) only converges satisfyingly for a few cases typically characterized by short core-hole lifetimes as given for the absorption by deep core electrons in high Z elements [8]. In most cases, however, convergence is poor and the multiple scattering expansion has to be carried out to very high or full order. In principle, this can be done by explicit matrix inversion of (1.8). Unfortunately, such a procedure is computationally very demanding and fast parallel Lanczos algorithms have been proposed and implemented to speed up calculations [8].

Another limitation of the current multiple scattering approach is given by the muffin-tin approach for the scattering potentials. This approximation usually works

well for sufficiently high photoelectron energies as given in the EXAFS region. In contrast, the photoelectron energies in the XANES region are small enough for the scattering to become sensitive to the details of the surrounding potentials. To avoid this limitation, several full potential approaches have been reported ([2, 5, 8] and references therein). Band structure calculations based on ground state density functional theory can also predict the properties of low energy excited states, however, self-energy effects are typically neglected. Core-hole effects can be included by a super-cell approach leading to significant improvements of the calculated spectra. Several full multiple scattering cluster methods represent approaches intermediate between band structure calculations and path expansion and have been used for a variety of XANES calculations ([7] and references therein).

Comparison of experimentally determined spectra with ab initio calculations and even structural fitting of XANES data, especially for small molecules and clusters, have made tremendous progress in recent years. Nevertheless, theoretical calculations are still less mature and satisfying than in the EXAFS region. However, given that XANES is sensitive to both the three-dimensional atomic arrangement and the density of unoccupied states, improving its theoretical description is a field of much current effort and further progress can be expected in the near future.

1.2.5 EXAFS

1.2.5.1 EXAFS Equation

The EXAFS is expressed in terms of the fine structure contribution

$$\chi(E) = \frac{\mu(E) - \mu_0(E)}{\mu_0(E)} \sim \frac{\mu(E) - \mu_0(E)}{\Delta\mu_0} \quad (1.10)$$

where the energy-dependent denominator is approximated by a constant typically chosen as the height of the absorption edge, $\Delta\mu_0 = \mu_0(E_0)$ with E_0 being the energy of the absorption threshold. Instead of using $\chi(E)$, the fine structure is usually written as a function of the photoelectron wave number $k = \sqrt{2m_e(E - E_0)/\hbar^2}$, where m_e stands for the electron mass and \hbar denotes Planck's constant divided by 2π . Using the *multiple scattering* path expansion described in Sect. 1.2.3, the fine structure contribution can be expressed as a sum over the scattering contributions arising from the various different paths

$$\begin{aligned} \chi(k) = \sum_j S_0^2 N_j \frac{|f_j(k)|}{k R_j^2} e^{-2R_j/\lambda(k)} e^{-2\sigma_j^2 k^2} \\ \times \sin[2k R_j + 2\delta_c(k) + \delta_j(k)] \end{aligned} \quad (1.11)$$

Paths with the same kinds of scattering atoms and a similar path length have been grouped under the index j . Equation (1.11) thus directly relates the EXAFS signal to the structural parameters N_j , R_j , and σ_j^2 which represent the number of such similar paths, the mean path length divided by two and the variation of all path lengths with index j , respectively. $f_j(k) = |f_j(k)|e^{i\delta_j(k)}$ represents the complex scattering amplitude while $\delta_c(k)$ stands for the phase shift experienced by the photoelectron wave in the potential of the absorbing atom. $\lambda(k)$ and S_0^2 denote the energy-dependent mean free path of the electron and the amplitude reduction factor, respectively.

Except for the factor S_0^2 , (1.11) was first derived by Sayers, Stern, and Lytle for *single scattering* paths using the plane-wave approximation [12]. It assumes that the distance between the absorber-backscatter pair is sufficiently large to treat the outgoing spherical wave as a plane wave once it reaches the backscattering atom. For *single scattering* events, all paths involving the same kind of scattering atom in the same coordination shell around the absorber are grouped together. The structural parameters N_j , R_j , and σ_j^2 then represent the coordination number, the mean value, and the variance of the corresponding absorber-scatterer distance distribution, respectively. In case of the first nearest neighbor shell, absorbing and scattering atoms are usually connected by a real physical bond, and R_j and σ_j^2 signify the mean value and variance of the bond length distribution. Equation (1.11) has become known as the ‘standard EXAFS equation’ and has founded the application of XAS as a tool for structural analysis.

For an accurate calculation of the fine structure contribution, however, multiple scattering paths, curved-wave effects and many-body interactions must be taken into account [7]. Nevertheless, $\chi(k)$ can still be expressed in the same form as the original EXAFS equation. This provides a convenient parameterization of the absorber environment in terms of structural parameters for single and multiple scattering paths. The other quantities of (1.11) implicitly contain the curved-wave and many-body effects of modern XAS theory as discussed below. The key features of the EXAFS equation are as follows:

- (i) As described in Sect. 1.1.2, the interference pattern depends on the photoelectron energy or wave number and on the distance between the absorbing and scattering atoms. This is given by the $\sin[2kR_j]$ term which causes the oscillatory nature of the fine structure contribution.
- (ii) The strength of the scattering and thus the magnitude of the EXAFS depend on the number and type of the scattering atoms, represented by the coordination number or degeneracy of paths N_j and the modulus of the scattering amplitude $|f_j(k)|$, respectively. Modern XAS theory replaces the original plane-wave scattering amplitude by an effective curved-wave scattering amplitude for either single or multiple scattering events. Apart from the dependence on k , the effective scattering amplitudes are also characterized by a weak dependence on r [2].
- (iii) The potential of the absorbing or scattering atom leads to a phase shift of the photoelectron wave represented by $\delta_c(k)$ and $\delta_j(k)$, respectively. The absorber potential acts twice on the photoelectron wave, once on the way out and once

on the way back. The resulting term $2\delta_c(k) + \delta_j(k)$ appears in the sine function of (1.11).

- (iv) The atoms in a particular coordination shell do not have exactly the same distance from the absorber. Differences are caused either by thermal vibrations (thermal disorder) or by structural variations in the interatomic distances (static disorder) and smear out the oscillations with increasing k . The phase difference in scattered waves due to a given difference in R_j increases with increasing k . This yields increased damping of the EXAFS at high wave numbers. In systems where the distance distributions exhibit only small asymmetry, Gaussian distributions with variance σ_j can be assumed. The term $e^{-2\sigma_j^2 k^2}$ in (1.11) then accounts for the k -dependent damping of the EXAFS oscillations. In analogy to X-ray diffraction, σ_j^2 is often called the EXAFS Debye-Waller factor.
- (v) The range that is probed by EXAFS is usually of the order of ten angstroms and is limited by the finite lifetime of the core hole and the finite mean free path of the photoelectron. The core-hole is eventually filled with an electron from a higher shell thereby emitting a fluorescence X-ray or an Auger electron while the photoelectron undergoes inelastic interactions with the surrounding material such as inelastic scattering and electron or plasmon excitation (extrinsic losses). The term $e^{-2R_j/\lambda(k)}$ in (1.11) accounts for the increasing decay of the photoelectron wave with increasing distance R_j . The mean free path is approximately given by $\lambda(k) \sim k/(|\text{Im } \Sigma| + \Gamma/2)$ and thus comprises the finite core-hole lifetime Γ and extrinsic losses calculated in terms of the complex self-energy Σ [8]. The damping of the fine structure contribution by both $\lambda(k)$ and σ_j^2 makes EXAFS a local probe and ensures the convergence of the multiple scattering path expansion in this regime.
- (vi) The one-electron approximation assumes that only a single electron participates in the absorption process. In reality, however, this is a many-body process and relaxation of the system in response to the sudden creation of the core-hole reduces the fine structure component. The corresponding amplitude reduction factor S_0^2 is, in principle, weakly energy dependent, particularly close to the absorption threshold. In the EXAFS region it can be taken as a constant to good approximation [8, 10].

1.2.5.2 Configurational Average

As already mentioned above, the sample contains an ensemble of slightly different atomic environments due to thermal and structural disorder. The EXAFS equation discussed above assumes Gaussian distance distributions with mean values R_j and standard deviations σ_j . For systems with significant asymmetry, a Gaussian function may no longer be an adequate approximation for the distance distribution and higher moments must be considered. EXAFS analysis based on a cumulant expansion was first proposed by Bunker [13]. Scattering from a coordination shell with a distance

distribution $\rho(R)$ yields

$$\begin{aligned}\chi(k) &= S_0^2 N \frac{|f(k)|}{k} \int_0^\infty \frac{e^{-2R/\lambda(k)}}{R^2} \sin[2kR + \delta(k)] \rho(R) dR \\ &= \text{Re} \left[\frac{1}{i} S_0^2 N \frac{|f(k)|}{k} e^{i\delta(k)} \int_0^\infty \frac{e^{-2R/\lambda(k)}}{R^2} e^{2ikR} \rho(R) dR \right]\end{aligned}\quad (1.12)$$

for each term j in (1.11) with $\delta(k) = 2\delta_c(k) + \delta_j(k)$. Assuming a narrow distribution with the mean value $\langle R \rangle$, the integral can be approximated by

$$\int_0^\infty \frac{e^{-2R/\lambda(k)}}{R^2} e^{2ikR} \rho(R) dR \sim \frac{e^{-2\langle R \rangle/\lambda(k)}}{\langle R \rangle^2} \int_0^\infty e^{2ikR} \rho(R) dR \quad (1.13)$$

where the integral on the right hand side corresponds to a Fourier transformation of the distance distribution and is called the characteristic function. It can be expressed in terms of the raw moments p_n or the cumulants C_n of the distance distribution

$$\int_0^\infty e^{2ikR} \rho(R) dR = \sum_{n=0}^\infty \frac{(2ik)^n}{n!} p_n = \exp \left[\sum_{n=0}^\infty \frac{(2ik)^n}{n!} C_n \right] \quad (1.14)$$

Although mathematically equivalent, the cumulant expansion converges much more rapidly than the expansion in terms of raw moments. Developing the sum in (1.14), using $C_0 = 0$ for normalized distributions, and neglecting cumulants higher than the fourth, (1.12) can be written as

$$\begin{aligned}\chi(k) &= S_0^2 N \frac{|f(k)|}{k} \frac{e^{-2\langle R \rangle/\lambda(k)}}{\langle R \rangle^2} e^{(-2k^2 C_2 + \frac{2}{3} k^4 C_4)} \\ &\quad \times \sin \left[2kC_1 - \frac{4}{3} k^3 C_3 + \delta(k) \right]\end{aligned}\quad (1.15)$$

This expression now allows the EXAFS to be analyzed in terms of the cumulants of the interatomic distance distribution: the first cumulant $C_1 = \langle R \rangle = R_j$ corresponding to the mean value, the second cumulant $C_2 = \sigma_j^2$ representing the variance and the third and fourth cumulants, C_3 and C_4 , denoting asymmetric and symmetric deviations from a Gaussian profile, respectively. For very small or Gaussian disorder, only the first two cumulants have to be considered and (1.15) corresponds to (1.11).

EXAFS samples the one-dimensional distance distribution $\rho(R)$ that results from an angular average over the three-dimensional distribution $\rho(\vec{R})$. Therefore, care has to be taken when comparing the cumulants of $\rho(R)$ with the three-dimensional

motion of the atoms or with structural parameters determined by other techniques such as X-ray diffraction (see Chap. 6).

For highly disordered systems, cumulants higher than the fourth may be necessary to adequately represent the distance distribution. In this case, the cumulant expansion is no longer a suitable description of the EXAFS and a different approach such as the one based on expressing the fine structure in terms of irreducible n -body interactions is more appropriate (see Chap. 9).

1.3 Experimental Aspects

1.3.1 Synchrotron Radiation

Most XAS experiments are performed at synchrotron sources due to the requirement of high X-ray intensities and a continuous energy spectrum [2]. Figure 1.4 shows the basic design of a modern synchrotron. Electrons produced in the source are first accelerated in a linear accelerator before their energy is further increased in the booster ring. From here they are transferred to the storage ring where they circulate over a million times each second, creating intensive electromagnetic radiation. Beamlines deliver the radiation to a number of end stations where it can be used for a variety of experimental techniques.

When a charged particle traverses a magnetic field it is forced to change its direction of motion thereby emitting electromagnetic radiation. In a synchrotron, the electrons are forced around the storage ring by a series of bending magnets [2]. The radiation thus created is characterized by a continuous energy spectrum over a wide range of wavelengths (from infrared to hard X-rays), high intensity, strong polarization and a pulsed nature. Modern synchrotron facilities also have additional elements, so-called insertion devices, placed in the straight sections between the

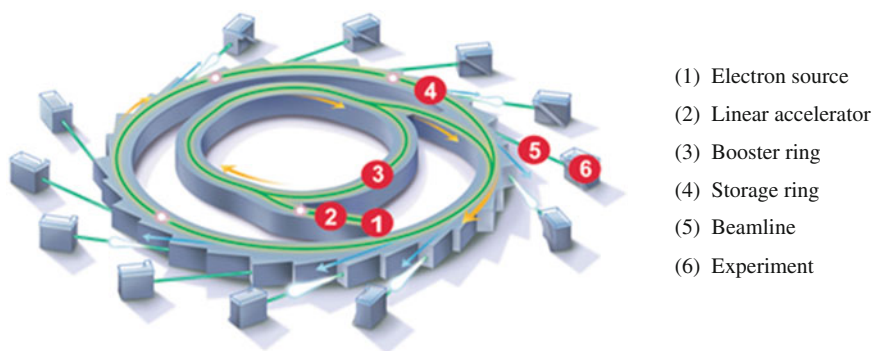


Fig. 1.4 Design of a modern synchrotron facility [14]

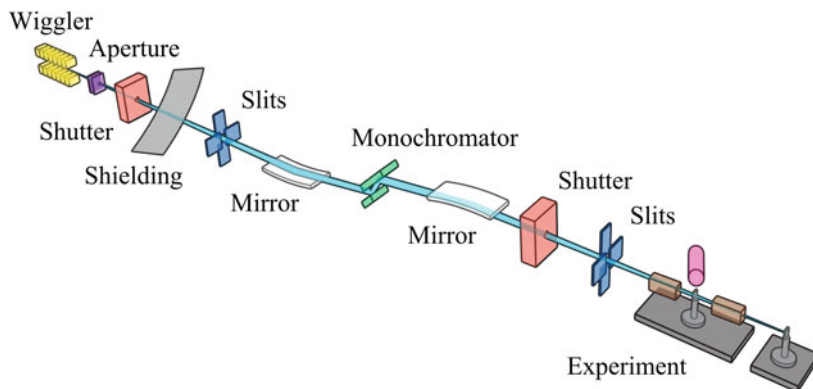


Fig. 1.5 Typical components of a modern XAS beamline [14]

bending magnets [2]. These devices constitute a series of alternating magnetic fields that force the electron beam to perform either strong (wiggler) or gentle (undulator) oscillations. The wiggler emits a broad beam of incoherent radiation characterized by increased intensity and a continuous energy spectrum extending to much higher X-ray energies compared to a bending magnet. The undulator emits a narrow beam of coherent radiation the intensity of which is amplified up to 10,000 times but only at certain energies. Based on these characteristics, the source (bending magnet, wiggler or undulator) best suited for a particular experimental technique is chosen.

Each beamline is usually configured to meet the requirements of a particular experimental technique [2]. Figure 1.5 depicts the various components of a typical modern XAS beamline. Mirrors are used to collimate and focus the beam while apertures and slits define its size. A double crystal monochromator is used to select X-rays of a very narrow energy band using the criterion for Bragg diffraction, $n\lambda = 2d \sin \theta$. Here, n is an integer, λ denotes the X-ray wavelength, d stands for the lattice spacing of the diffracting crystal and θ represents the angle under which the beam is incident on the crystal. Energies that satisfy the Bragg condition with $n \geq 2$ are called “harmonics” and have to be removed from the beam. This can be achieved by slightly detuning the monochromator which decreases the transmission of harmonics significantly more than that of the primary energy. Alternatively, X-ray mirrors can be used that only reflect energies below a critical value. With such an experimental arrangement, the absorption coefficient can be measured as a function of X-ray energy.

1.3.2 Experimental Setup

In general, the absorption coefficient can be detected either directly by measuring the intensities of incoming and transmitted beam (transmission mode) or indirectly by

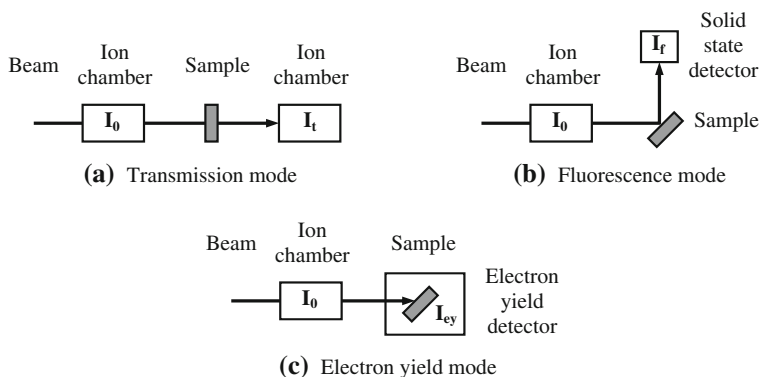


Fig. 1.6 Schematic of the experimental setup for the different XAS detection modes

measuring the intensity of the incoming beam and of the decay products such as fluorescent X-rays or Auger electrons (fluorescence or electron yield mode). The experimental setup for all three cases is shown schematically in Fig. 1.6 [2]. Alternatively, X-ray excited optical luminescence (XEOL) measures electromagnetic emissions in the optical range following X-ray absorption and is described in Chaps. 11 and 13.

1.3.2.1 Transmission Mode

In transmission mode both the incoming and the transmitted beam, I_0 and I_t , respectively, are measured by ion chambers and the absorption coefficient can be obtained according to (1.1) [2, 4]. Detecting the voltage or current generated in the ion chamber counting chain is inherently simpler than detecting single photons with a solid state detector often used for fluorescence measurements (see below). Using the same type of detector for I_0 and I_t also has the advantage of having a common energy dependence. However, transmission measurements require concentrated samples such that the difference between I_0 and I_t is significantly larger than the variation due to counting statistics. Furthermore, samples must be highly homogeneous, of constant thickness and free of pinholes. One means to prepare a sample that satisfies these requirements is to crush up an appropriate amount of material and mix it with a suitable binder such as boron nitride or cellulose. Once a fine, homogeneous powder is obtained, it is compacted into the small hole of a sample holder or pressed into a pellet and sealed on both sides with Kapton tape.

1.3.2.2 Fluorescence Mode

The intensity of the incoming beam I_0 is again measured by an ion chamber while the intensity of the characteristic fluorescence X-rays is usually detected by an energy-dispersive Si or Ge solid state detector [2]. The intensity of this fluorescence line is

proportional to the absorption caused by the element under investigation, however, the relation is more complicated than for transmission measurements. So-called “self-absorption” effects must be taken into account especially for thick or concentrated samples [15]. Furthermore, detecting the fluorescence signal is also more complicated than measuring the transmitted intensity since the characteristic X-rays have to be isolated from other X-rays, particularly the elastically scattered beam itself. While Si and Ge solid state detectors are capable of the required energy discrimination they suffer from limited count rates. To improve the signal-to-noise ratio several independent detectors are coupled in an array to form multiple-element detectors with up to 100 channels [14]. Nevertheless, the big advantage of the fluorescence mode is the ability to study samples not suitable for measurement in transmission mode such as highly dilute and non-homogeneous samples.

1.3.2.3 Electron Yield Mode

Instead of detecting the fluorescent X-rays, one can also measure the electrons emitted from the sample such as the photoelectrons themselves, secondary electrons and Auger electrons. To that end the sample is situated inside the detector and the electrons are collected by suitable electrodes [2]. Given the relatively short mean free path of the electrons this technique is surface sensitive and does not suffer from the “self-absorption” effects mentioned above for the fluorescence mode [2, 4]. It is also beneficial for measuring samples in the soft X-ray regime where the filling of the core-hole is accompanied mainly by Auger electron production and only to a much lesser extent by fluorescence X-ray emission.

1.3.2.4 Specialized Experimental Techniques

A number of specialized experimental techniques have been developed to capitalize on additional physical effects or to accommodate the particular nature of a large variety of samples. Very thin films and nanostructures can be studied by grazing incidence measurements where the angle between the incoming X-ray beam and the sample surface is typically only a few degrees, equivalent to a few tens of milliradians [2, 5]. The penetration depth of the X-rays is then strongly reduced yielding a highly surface sensitive measurement. Usually, the emitted fluorescent X-rays are recorded with the detector placed at 45° with respect to the sample surface. By varying the angle of incidence, information about the absorption coefficient can be obtained for different depths. If the angle between the incoming beam and the sample surface is reduced below the critical angle of the material, typically a few milliradians, total external reflection will occur. The X-ray wave field is now confined to the immediate surface and the penetration depth is in the order of some nanometers. Detecting the intensity of the reflected beam then provides information about the absorption coefficient. However, care has to be taken when using this approach as the reflectivity depends on both the real and the imaginary part of the index of refraction yielding

a complicated relation between the measured signal and the absorption coefficient (see also Chap. 12).

Atomic-scale structural information of crystalline samples can also be obtained from X-ray diffraction anomalous fine structure (DAFS) studies where the intensity of a particular Bragg reflection is measured as a function of X-ray energy [16, 17]. Due to the causal relationship between the real and imaginary parts of the atomic scattering amplitude, the energy-dependent variation of the scattering signal contains the same structural information as the X-ray absorption fine structure. In contrast to XAS, DAFS can provide site or spatial selectivity if the element of interest occupies inequivalent sites that have different structure factor contributions or if different spatial regions of the sample produce diffraction peaks at separate locations in reciprocal space [16]. The Bragg reflections of a strained $\text{In}_x\text{Ga}_{1-x}\text{As}$ layer, for example, differ from those of the GaAs substrate thus allowing the study of the Ga and As environments in the ternary thin film without interference from the substrate [17]. Extracting structural information from the DAFS signal is, however, more complicated than in the case of XAS and usually requires very thin samples [16, 17]. Examples for the application of DAFS can be found in Chaps. 10 and 13.

As described in Sect. 1.2.1, the transition matrix element and hence the absorption coefficient depend on the orientation of the absorbing and scattering atom pair with respect to the X-ray polarization. For single crystal samples, such as strained epitaxial thin films or oriented nanostructures, the recorded signal therefore depends on the angle between the sample normal and the X-ray beam. Performing angle-dependent measurements then yields information about the structural parameters parallel and perpendicular to the sample normal as discussed in Chaps. 3, 5, 13 and 16.

For some applications, such as time-resolved studies (see e.g. Chap. 13), very short scanning times are required. During conventional XAS experiments, the monochromator is set at a certain angle corresponding to a specific X-ray energy and the intensities of interest are recorded before the monochromator is moved to the next setting. The scanning speed is thus limited by the time needed to move and settle the monochromator and to measure the signal. In contrast, scanning times can be dramatically reduced by using a monochromator moving with constant velocity and fast data acquisition systems [18, 19]. A full scan performed with such a quickXAS setup may take tens of seconds compared to 30–60 minutes for conventional scans. Even faster measurements in the order of one second or less can be realized by energy dispersive XAS where a polychromatic beam is incident on the sample and then diverges onto a position sensitive detector such as a photodiode array [18, 19]. The spectrum is thus recorded simultaneously and the time needed is limited only by the response time of the detector and the number of scans required for a sufficient signal to noise ratio.

Recent progress in the field of X-ray micro beams also opens up new possibilities, particularly for the study of inhomogeneous or heterogeneous materials and nanostructures (see e.g. Chap. 13). Brilliant synchrotron sources and specialized beam line optics such as compound refractive lenses, Fresnel zone plates and Kirkpatrick-Baez mirrors now provide X-ray beams with spot sizes of the order of tens of nanometers [20]. Structural parameters can thus be studied with a

sub-micron spatial resolution. Often these microXAS measurements are combined with other techniques such as compositional analysis using micro X-ray fluorescence to obtain a more comprehensive picture of the material investigated.

1.4 Data Analysis

There exists a variety of ways to analyze XAS data and a large number of codes and programs are available. In general, data from the XANES and EXAFS region are analyzed separately. This is partly due to the different information contained in both spectral regions and partly due to the fact that theoretical modeling for XANES is not yet as advanced as it is for EXAFS. Even with the progress made over recent years, simultaneous calculation of the fine structure in both regions is numerically impractical thus favoring a separate analysis.

An important point common to both spectral regions, however, is the calibration of the energy scale and the alignment of different spectra. The beamline monochromator is calibrated with a known reference, often a thin metal foil, at each absorption edge. Ideally, this reference is then measured simultaneously with each sample of interest. In transmission mode this can be easily achieved by placing the reference between the second and a third ion chamber that detect the X-ray intensity incident on and transmitted through the reference, respectively. These reference spectra can then be used to align the energy scales of the samples of interest. In fluorescence mode this approach is often not feasible due to a thick absorbing substrate of the sample. It is then important to check the stability of the energy calibration at suitable intervals. Correct alignment of the sample spectra is crucial for the determination of edge shifts in the XANES and for bond length determination from EXAFS. Furthermore, thickness and “self-absorption” effects distort the amplitude of the fine structure and must be avoided or corrected for a meaningful analysis.

1.4.1 XANES

The absorption edge is often comprised of intense absorption peaks (white lines) and pre-edge features [2]. The white line results from strong transitions to final states confined to the near vicinity of the absorbing atom. These can be partially filled or empty bound states, sensitive to chemical bonding and the oxidation state of the absorbing atom, or low energy continuum states confined by strong multiple scattering, sensitive to the three dimensional structure surrounding the absorber. Pre-edge features are typically taken as a sign of broken inversion symmetry and thus also provide structural information. Small energy shifts of the absorption edge itself can be caused by charge transfer between the absorber and the neighboring atoms. More pronounced shifts can result from changes in the first nearest neighbor bond lengths [2].

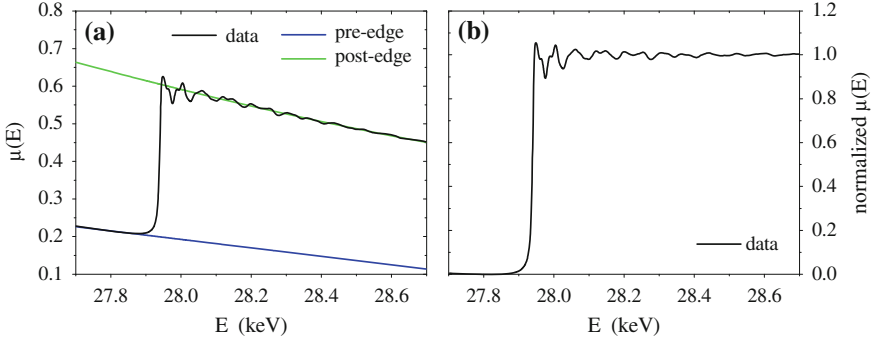


Fig. 1.7 **a** Raw $\mu(E)$ data measured at the In K -edge of crystalline InP together with the fitted pre-edge and post-edge lines. **b** Normalized $\mu(E)$ obtained from the spectrum in panel (a)

The first step in XANES analysis is the normalization of spectra [4]. To that end, the spectrum in the energy region below the absorption edge is fitted by a linear pre-edge line as shown in Fig. 1.7a. The spectrum well above the absorption edge is typically approximated by a quadratic post-edge line. The edge step $\Delta\mu_0$ is then obtained as the difference between pre-edge and post-edge lines at the absorption threshold E_0 . A normalized XANES spectrum as shown in Fig. 1.7b is then obtained by subtracting the pre-edge line from the measured spectra over the whole energy range, dividing by the step height $\Delta\mu_0$ and flattening the spectra above threshold to account for the different slopes of pre-edge and post-edge lines. The resulting normalized spectrum equals zero below the edge, exhibits a step height of one and oscillates around this value for energies above E_0 . Normalization thus removes effects of sample thickness and concentration and allows the direct comparison of different samples and measurements.

Comparing the spectra of the samples of interest with those of known standards already yields some qualitative assessment of the chemical and structural environment of the absorbing atom, provided the spectra of the standards are sufficiently different from each other. The analysis can be quantified by linear combination fitting. The spectrum of the sample of interest is modeled by weighting the spectrum of each known standard i with a factor f_i and adding them together

$$\mu_{calc} = \sum_i f_i \mu_i \quad (1.16)$$

The factors f_i represent the fraction with which each standard is present in the sample and are obtained by minimizing the difference between the calculated and measured spectrum. Ideally, they should sum to one. However, structural disorder can sometimes broaden the XANES features and the sum rule needs to be relaxed in these cases [4]. Linear combination fitting works well if the number of potential chemical and structural environments for the absorbing atom in the sample, and thus the number of standards, is small and if the spectra of these standards exhibit unique

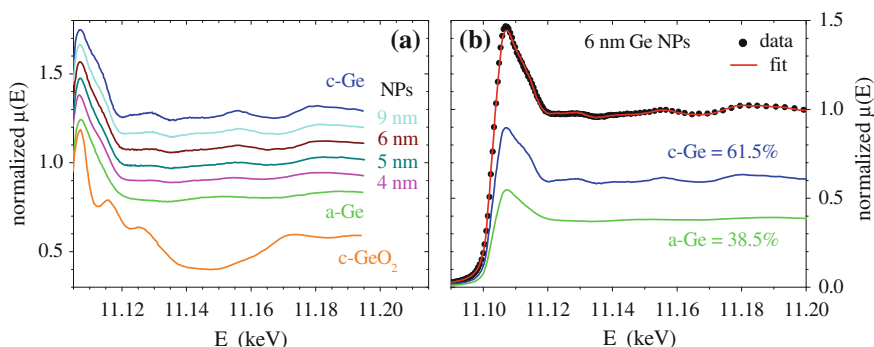


Fig. 1.8 **a** Ge K -edge XANES spectra for bulk crystalline Ge (c-Ge), amorphous Ge (a-Ge) and crystalline GeO₂ (c-GeO₂) compared with those for different sizes of Ge nanoparticles (NPs) embedded in a SiO₂ matrix. **b** Linear combination fitting of a nanoparticle spectrum with bulk crystalline and amorphous Ge standards [21]

features that allow to differentiate between them. Consequently, linear combination fitting is severely limited if a large number of possible standards has to be considered and if the spectra of different standards are very similar to each other.

As an example, Fig. 1.8a compares XANES spectra for bulk standards (crystalline Ge, amorphous Ge and crystalline GeO₂) with that for different sizes of Ge nanoparticles embedded in SiO₂ [21]. The features apparent in the spectra of the two crystalline standards stem from multiple scattering effects while, in contrast, the spectrum for the amorphous standard is effectively featureless. The latter demonstrates how the structural disorder inherent in the amorphous phase significantly impacts (diminishes) multiple scattering contributions. The nanoparticle spectra show no evidence of an oxide component and the crystalline-Ge-like features weaken as the nanoparticle size decreases. Figure 1.8b shows linear combination fitting of the spectrum for Ge nanoparticles of 6 nm diameter using the bulk crystalline and amorphous Ge standards. Clearly the XANES spectrum is well fitted with the given combination of standards. Within a Ge nanoparticle, Ge atoms are thus in either a crystalline or amorphous environment. This result was considered evidence for an amorphous-like Ge layer of constant thickness separating the crystalline Ge nanoparticle core and the amorphous SiO₂ matrix [21]. Ge nanoparticles are discussed in detail in Chap. 10.

A related technique is principal component analysis where a set of related samples of interest is analyzed in terms of characteristic principle components present in the samples. Interpretation of the results can, however, be difficult as the principal components are statistical abstractions and do not need to represent any physical standards [4].

Characteristic features such as white lines or pre-edge features can also be quantified by peak fitting procedures. To that end, the absorption edge itself is typically approximated by an arctangent function while the peaks are modeled by Lorentzian lines convoluted with a Gaussian function (Voigt function) to account for experimental broadening [2]. Such an analysis could yield, for example, the change in

edge position related to a change in first nearest neighbor distances for a series of samples or the fraction of different oxidation states (characterized by different white line positions) of the absorbing atom within a sample [4].

With the progress of XAS theory and the improvement of numerical codes (see Sect. 1.2.4), comparison of calculated and measured spectra gains more and more importance as an analytical tool. Currently, the aim is mostly to refine the parameters of a single chemical and structural environment of the absorbing atom but characterization of multicomponent samples based on theoretical calculations may well become possible in the future.

1.4.2 EXAFS

The first step in EXAFS analysis is to isolate the fine structure $\chi(k)$ from the absorption background [4]. To that end, the spectrum is fitted with a pre-edge and post-edge line as already described in Sect. 1.4.1. The pre-edge line is again subtracted from the spectrum over the whole energy range. The absorption background $\mu_0(E)$ is then typically approximated by a spline function that approaches the post-edge line at energies well beyond the absorption edge as shown in Fig. 1.9a. The difference between the absorption coefficient $\mu(E)$ and the background $\mu_0(E)$ is normalized with respect to the step height $\Delta\mu_0$ yielding the fine structure $\chi(E)$. To convert the energy E to the photoelectron wave number $k = \sqrt{2m_e(E - E_0)}/\hbar$, the threshold energy E_0 is needed. Experimentally, E_0 is typically taken as the maximum of the derivative of $\mu(E)$ with respect to E or as the energy corresponding to the half of the step height [2]. This choice is somewhat arbitrary and the chosen E_0 may not be identical to the actual absorption threshold. This does not pose a major problem for the analysis, however, as long as E_0 is chosen consistently for all samples under investigation (see below). Figure 1.9b plots $\chi(k)$ isolated from the data shown in panel (a) and weighted with k^3 to emphasize the data at higher k . Depending on the sample and the absorber-backscatterer pair, different k -weights may be chosen.

The next step is usually to Fourier transform the data into R -space [2, 4]. Fourier transformation (FT) of the EXAFS provides a means to visualize different scattering contributions and is often used during analysis. The benefit of such a procedure was first shown by Sayers et al. [12]. When Fourier transformed, different scattering contributions with a large difference in R_j and small values for σ_j^2 produce well separated peaks with amplitudes approximately proportional to N_j/σ_j . However, as $\lambda(k)$, $|f_j(k)|$, and $\delta_j(k)$ are complicated functions of k , the FT of the EXAFS cannot be expressed in a simple analytical form and may differ significantly from the radial distribution function [1]. Furthermore, different k -weights might be used and a smooth window function is usually applied to account for the finite data range. Nevertheless, EXAFS results are typically presented as the magnitude of the FT due to the illustrative character of such a plot. Figure 1.9b shows a window function of the Hanning type and Fig. 1.9c plots the magnitude of the resulting FT. Distinct peaks due to different scattering contributions are readily apparent. The first peak,

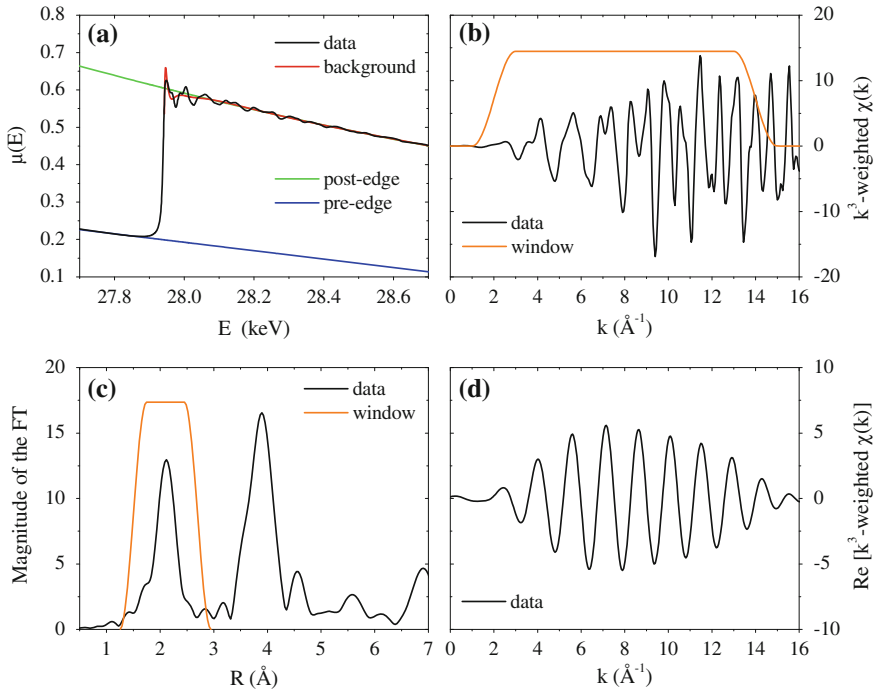


Fig. 1.9 **a** Raw $\mu(E)$ data measured at the In *K*-edge of crystalline InP together with the fitted pre-edge and post-edge lines and the background function. **b** k^3 -weighted $\chi(k)$ obtained after background removal and conversion from energy scale to photoelectron wave number scale. **c** Magnitude of the Fourier transformation (FT) obtained from the k^3 -weighted $\chi(k)$ using the smooth Hanning window plotted in panel (b). **d** Real part of the back-transformed data for the window plotted in panel (c) selecting the first nearest neighbor scattering peak

corresponding to scattering of the photoelectron wave at first nearest neighbor atoms, is usually well isolated. In contrast, the scattering contributions from higher coordination shells often overlap and a complicated peak structure may result. Furthermore, one should remember that the FT is a complex function and both magnitude and phase (or alternatively, real and imaginary part) have to be considered for the full information content.

A back-transformation can be used to isolate different scattering contributions if their signals are well separated in R -space. This methodology has been extensively used for the analysis of first nearest neighbor scattering by the Ratio Method (see below). However, it usually fails for higher coordination shells due to the overlap of different scattering contributions. Figure 1.9c shows a Hanning window selecting only the first nearest neighbor scattering peak. The real part of the resulting back-transformed k -spectra is plotted in Fig. 1.9d.

1.4.2.1 Ratio Method

Analysis using the Ratio Method is based on the EXAFS equation and the cumulant expansion and yields the differences in structural parameters between the sample of interest and a known reference. Expressing the fine structure of a single scattering contribution in terms of its amplitude $A(k)$ and phase $\Phi(k)$, $\chi(k) = A(k) \sin \Phi(k)$, (1.12) yields

$$A(k) = S_0^2 N \frac{|f(k)|}{k} \left| \int_0^\infty \frac{e^{-2R/\lambda(k)}}{R^2} e^{2ikR} \rho(R) dR \right| \quad (1.17)$$

$$\Phi(k) = \delta(k) + \arg \left[\int_0^\infty \frac{e^{-2R/\lambda(k)}}{R^2} e^{2ikR} \rho(R) dR \right] \quad (1.18)$$

The integral in both terms represents the FT of the *effective* distance distribution $\rho'(R) = \rho(R)e^{-2R/\lambda(k)}/R^2$ [13]. Using a cumulant expansion similar to (1.14), the amplitude and phase can be written as

$$A(k) = S_0^2 N \frac{|f(k)|}{k} \exp \left[C'_0 - 2k^2 C'_2 + \frac{2}{3} k^4 C'_4 \right] \quad (1.19)$$

$$\Phi(k) = \delta(k) + 2kC'_1 - \frac{4}{3}k^3 C'_3 \quad (1.20)$$

where C'_n denotes the cumulants of the effective distribution and orders higher than $n = 4$ have been neglected. In contrast to C_0 , C'_0 does not vanish as the effective distribution is generally not normalized. It can be estimated by [22]

$$C'_0 = -2 \frac{C'_1}{\lambda(k)} - 2 \ln C'_1 \quad (1.21)$$

The relation between C'_1 and C_1 is approximately given by [22]

$$C'_1 = C_1 - 2 \frac{C_2}{C_1} \left(1 + \frac{C_1}{\lambda(k)} \right) \quad (1.22)$$

Experimentally, $\lambda(k)$ is usually taken as a constant. For $n \geq 2$, the difference between the effective and the real cumulants is typically within the experimental uncertainty and $C'_n = C_n$ is assumed.

If the chemical and structural environment of the absorbing atom in the sample of interest (index s) and the reference (index r) is similar, such that $S_{0,s}^2 = S_{0,r}^2$ and

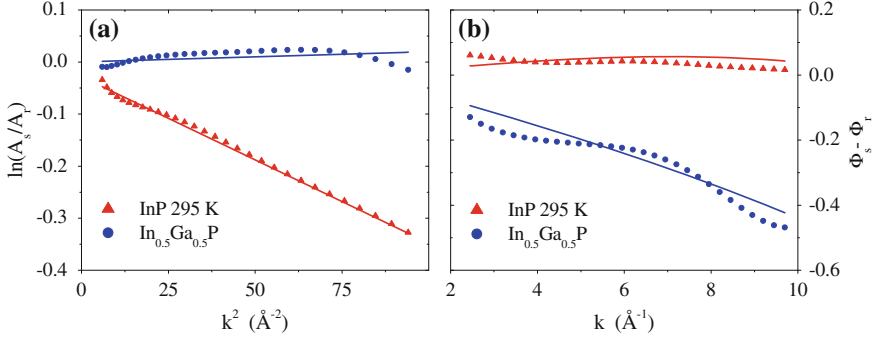


Fig. 1.10 Ratio method analysis of the samples InP measured at 295 K and $\text{In}_{0.5}\text{Ga}_{0.5}\text{P}$ measured at 20 K compared to the reference of InP measured at 20 K. **a** Logarithm of the amplitude ratio, in $|A_s(k)/A_r(k)|$, plotted versus k^2 and **b** phase difference $\Phi_s(k) - \Phi_r(k)$ plotted versus k where s and r denote the sample and the reference, respectively

$f_s(k) = f_r(k)$, comparison of amplitude and phase yields

$$\ln \left| \frac{A_s(k)}{A_r(k)} \right| = \ln \frac{N_s}{N_r} + \Delta C'_0 - 2k^2 \Delta C'_2 + \frac{2}{3}k^4 \Delta C'_4 \quad (1.23)$$

$$\Phi_s(k) - \Phi_r(k) = 2k \Delta C'_1 - \frac{4}{3}k^3 \Delta C'_3 \quad (1.24)$$

These differences $\Delta C'_n = C'_{n,s} - C'_{n,r}$ in the effective cumulants can then be determined from polynomial fits. As an example, Fig. 1.10a, b plot the logarithm of the amplitude ratio and the phase difference, respectively, obtained from a study of the In K -edge of InP measured at 295 K and $\text{In}_{0.5}\text{Ga}_{0.5}\text{P}$ measured at 20 K. The reference is in both cases InP measured at 20 K. The spectra were processed and Fourier transformed as described above yielding the amplitude and phase of the back-transformed first nearest neighbor scattering contribution. For InP measured at two different temperatures, the logarithm of the amplitude ratio is strongly sloped indicative of a significant increase of $C'_2 = C_2$ for 295 K compared to 20 K. This increase is caused by increased thermal disorder yielding a larger variance of the distance distribution. In contrast, the slope is basically zero for $\text{In}_{0.5}\text{Ga}_{0.5}\text{P}$ demonstrating a similar width of the distance distribution in binary and ternary. Regarding the phase difference, only a small increase of C'_1 is noted for InP measured at 295 K compared to InP measured at 20 K while the strong slope for $\text{In}_{0.5}\text{Ga}_{0.5}\text{P}$ results from a significant reduction of C'_1 compared to InP. Increasing the measurement temperature thus only slightly increases the average In-P distance in InP whereas alloying with GaP significantly reduces the value of C_1 (see also Chaps. 2 and 6).

The advantage of the Ratio Method is that it is a model independent approach that does not assume any structure a priori. It analyzes the differences in structural parameters between a sample and a reference and thus avoids the need to explicitly

know the scattering amplitudes and phase shifts. Due to this comparative nature, many experimental effects also cancel out. It does, however, assume that the chemical and structural environment of the absorbing atom is sufficiently similar in the sample and the reference. In many cases, this requirement is satisfied but there may be samples for which it is difficult to find a suitable reference. Another major limitation of the Ratio Method is the need to have scattering contributions well isolated in R -space which usually limits the analysis to the first coordination shell.

1.4.2.2 Path Fitting

Path fitting is another approach to EXAFS analysis provided for example by the IFEFFIT code [23] and the corresponding user interfaces ATHENA and ARTEMIS [24]. It is a model-dependent approach based on the cumulant expansion of the different single and multiple scattering paths and requires some pre-existing knowledge about the system under investigation. The analysis starts with a model structure that specifies the absorbing atom and the position and type of the surrounding atoms that are to be considered in the fitting procedure. Effective scattering amplitudes and phase shifts for the various single and multiple scattering paths are then calculated with the FEFF code [9]. The calculations are based on the multiple scattering approach described in Sect. 1.2.3 and include polarization dependence, curved-wave effects, core-hole effects and many-body interactions. Scattering paths are sorted with respect to their effective distance and their importance given by the scattering amplitude is listed. Usually, single scattering paths are stronger than multiple scattering paths of similar length. Nevertheless, some multiple scattering paths may be strong enough that an accurate representation of the experimental spectrum is only possible if they are considered in the fit. The selection of relevant paths to be included in the fitting procedure may vary depending on the system studied, the quality of the data and the aim of the investigation.

Figure 1.11a, b show the most prominent scattering paths calculated for absorption at the In K -edge of InP and $\text{In}_{0.5}\text{Ga}_{0.5}\text{P}$, respectively. For InP, the strongest multiple scattering (MS) path is also plotted leading from the In absorber to a second nearest neighbor In atom, then to a first nearest neighbor P atom and back to the absorber. For $\text{In}_{0.5}\text{Ga}_{0.5}\text{P}$, no multiple scattering paths were included in Fig. 1.11b for the sake of clarity. The complex Fourier transformed paths can add up constructively or destructively depending on their phases. As an example, the peak at $R \sim 4 \text{ \AA}$ in Fig. 1.11a is smaller for the sum of all paths than for the second nearest neighbor In path alone, highlighting the importance of considering the full information content of the FT.

The structural parameters of the selected paths are refined in a least-squares fit to the processed experimental data. The first four cumulants $C_1 = \langle R \rangle$, $C_2 = \sigma^2$, C_3 , and C_4 can be fixed, restrained or varied freely for each scattering path depending on the system studied, the quality of the data and the aim of the investigation. Fitting is often performed with multiple k -weights to minimize the correlation between the different parameters. Neither the E_0 value chosen during data processing nor the

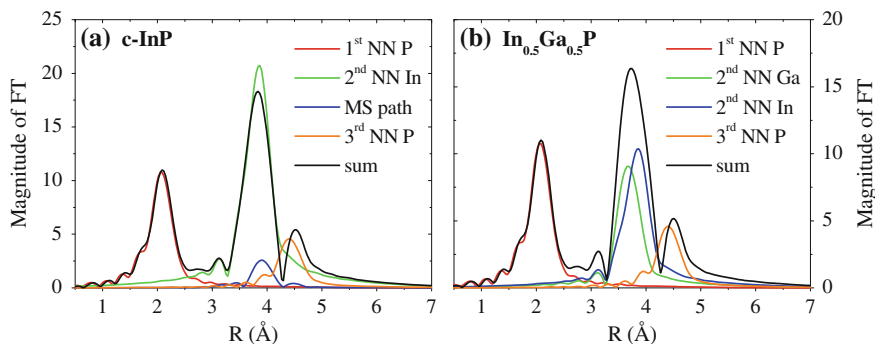


Fig. 1.11 Most important theoretical scattering paths for absorption at the In K -edge of **a** InP and **b** $\text{In}_{0.5}\text{Ga}_{0.5}\text{P}$. The magnitude of the FT is plotted as a function of radial distance R for the different scattering path and their complex sum

theoretically calculated E_0 necessarily correspond to the actual absorption threshold. Therefore, an additional fitting parameter accounts for the difference between experimental effects such as data normalization. Often, E_0 and S_0^2 are determined from a suitable reference and are then kept constant during the analysis of the sample of interest.

The biggest advantage of the path fitting approach is the ability to analyze the structural parameters beyond the first coordination shell which often contain crucial information not available from the first nearest neighbor environment. Furthermore, the calculation of the scattering paths takes into account the full k -dependencies of all parameters and yields the cumulants of the *real* interatomic distance distribution. Path fitting analysis does not require the measurement of a reference with similar chemical and structural environment of the absorbing atom, although, it is advantageous for the determination of E_0 and S_0^2 if possible. A major drawback of the path fitting approach is the need for an initial structural model and thus the need for some pre-existing knowledge about the sample structure. Moreover, the quality of the results obviously depends strongly on the quality of the theoretical calculations. However, tremendous progress has been made in this area in recent years and, usually, shortcomings in the theory no longer pose a major problem.

1.4.2.3 Alternative Approaches

Other codes, with alternative approaches, have been developed for the analysis of XAS data and include, for example, EXCURVE [25] and GNXAS [10, 11]. Utilization of these and other packages can be advantageous for particular materials and forms thereof. The GNXAS code, for example, describes XAS data as a series of integrals over n -body distribution functions and is well suited to disordered systems including amorphous solids and liquids (see Chaps. 9 and 14).

1.5 Conclusions

We have sought to introduce and describe the fundamentals of XAS theory and experiment and, in doing so, lay the foundation for the more detailed chapters that now follow. As the reader will soon appreciate, these chapters demonstrate and reinforce the ever-expanding utilization of the XAS technique for the characterization of semiconductor materials.

References

1. D.C. Koningsberger, R. Prins, *X-ray Absorption: Principles, Applications, Techniques of EXAFS, SEXAFS and XANES* (Wiley, New York, 1988)
2. G. Bunker, *Introduction to XAFS* (Cambridge University Press, Cambridge, 2010)
3. S. Calvin, *XAFS for Everyone* (CRC Press, Taylor & Francis, Boca Raton, 2013)
4. S.D. Kelly, D. Hesterberg, B. Ravel, Analysis of soils and minerals using X-ray absorption spectroscopy, in *Methods of Soil Analysis—Part 5: Mineralogical Methods*, Soil Science Society of America Book Series No. 5, Madison (2008)
5. F. Boscherini, X-ray absorption fine structure in the study of semiconductor heterostructures and nanostructures, in *Characterization of Semiconductor Heterostructures and Nanostructures*, ed. by C. Lamberti (Elsevier, Amsterdam, 2008)
6. J. Als-Nielsen, D. McMorrow, *Elements of Modern X-ray Physics* (Wiley, Chichester, 2001)
7. J.J. Rehr, R.C. Albers, *Rev. Mod. Phys.* **72**, 621 (2000)
8. J.J. Rehr, A.L. Ankudinov, *Coord. Chem. Rev.* **249**, 131 (2005)
9. J.J. Rehr, J.J. Kas, F.D. Vila, M.P. Prange, K. Jorissen, *Phys. Chem. Chem. Phys.* **12**, 5503 (2010)
10. A. Filipponi, A. Di Cicco, C.R. Natoli, *Phys. Rev. B* **52**, 15122 (1995)
11. A. Filipponi, A. Di Cicco, *Phys. Rev. B* **52**, 15135 (1995)
12. D.E. Sayers, E.A. Stern, F.W. Lytle, *Phys. Rev. Lett.* **27**, 1204 (1971)
13. G. Bunker, *Nucl. Instrum. Methods.* **207**, 437 (1983)
14. Australian Synchrotron website (<http://www.synchrotron.org.au/>)
15. C.H. Booth, F. Bridges, *Phys. Scripta* **T115**, 202 (2005)
16. H. Stragier, J.O. Cross, J.J. Rehr, L.B. Sorensen, C.E. Bouldin, J.C. Woicik, *Phys. Rev. Lett.* **69**, 3064 (1992)
17. J.C. Woicik, J.O. Cross, C.E. Bouldin, B. Ravel, J.G. Pellegrino, B. Steiner, S.G. Bompadre, L.B. Sorensen, K.E. Miyano, J.P. Kirkland, *Phys. Rev. B* **58**, R4215 (1998)
18. A.J. Dent, *Top. Catal.* **18**, 27 (2002)
19. R. Frahm, J. Stötzl, D. Lützenkirchen-Hecht, *Synchrotron Rad. News* **22**, 6 (2009)
20. G.E. Ice, J.D. Budai, J.W.L. Pang, *Science* **334**, 1234 (2011)
21. L.L. Araujo, R. Giulian, D.J. Sprouster, C.S. Schnohr, D.J. Llewellyn, P. Kluth, D.J. Cookson, G.J. Foran, M.C. Ridgway, *Phys. Rev. B* **78**, 094112 (2008)
22. G. Dalba, P. Fornasini, R. Grisenti, D. Pasqualini, D. Diop, F. Monti, *Phys. Rev. B* **58**, 4793 (1998)
23. M. Newville, *J. Synchrotron Radiat.* **8**, 322 (2001)
24. B. Ravel, M. Newville, *J. Synchrotron Radiat.* **12**, 537 (2005)
25. N. Binstead, J.W. Campbell, S.J. Gurman, P.C. Stephenson, *The Excurve Programs* (Daresbury Laboratory, England, 1991)

X-Ray Absorption Spectroscopy of Semiconductors

Schnohr, C.S.; Ridgway, M. (Eds.)

2015, XVI, 361 p. 185 illus., 86 illus. in color., Hardcover

ISBN: 978-3-662-44361-3